

PAPER • OPEN ACCESS

Phase-coherent loops in selectively-grown topological insulator nanoribbons

To cite this article: Jonas Kölzer *et al* 2020 *Nanotechnology* **31** 325001

View the [article online](#) for updates and enhancements.

Recent citations

- [Reappearance of first Shapiro step in narrow topological Josephson junctions](#)
Daniel Rosenbach *et al*
- [Quantum Transport in Topological Surface States of Selectively Grown Bi₂Te₃ Nanoribbons](#)
Daniel Rosenbach *et al*



The Electrochemical Society
Advancing solid state & electrochemical science & technology
2021 Virtual Education

Intensive Short Courses

Sun, Oct 10 & Mon, Oct 11



Providing students and professionals with in-depth education on a wide range of topics

Early registration deadline: Sep 13, 2021

Register early and save!



Phase-coherent loops in selectively-grown topological insulator nanoribbons

Jonas Kölzer^{1,2,4} , Daniel Rosenbach^{1,2,4} , Christian Weyrich^{1,2}, Tobias W Schmitt^{1,2}, Michael Schleenvoigt^{1,2}, Abdur Rehman Jalil^{1,2}, Peter Schüffegen^{1,2} , Gregor Mussler^{1,2} , Vincent E Sacksteder IV³, Detlev Grützmacher^{1,2} , Hans Lüth^{1,2}  and Thomas Schäpers^{1,2} 

¹ Peter Grünberg Institute (PGI-9), Forschungszentrum Jülich, 52425 Jülich, Germany

² JARA-Fundamentals of Future Information Technology, Jülich-Aachen Research Alliance, Forschungszentrum Jülich and RWTH Aachen University, Germany

³ Wittenberg University, Springfield, Ohio, 45504, United States of America

E-mail: th.schaeppers@fz-juelich.de

Received 14 January 2020, revised 14 March 2020

Accepted for publication 15 April 2020

Published 21 May 2020



Abstract

We succeeded in the fabrication of topological insulator $(\text{Bi}_{0.57}\text{Sb}_{0.43})_2\text{Te}_3$ Hall bars as well as nanoribbons by means of selective-area growth using molecular beam epitaxy. By performing magnetotransport measurements at low temperatures information on the phase-coherence of the electrons is gained by analyzing the weak-antilocalization effect. Furthermore, from measurements on nanoribbons at different magnetic field tilt angles an angular dependence of the phase-coherence length is extracted, which is attributed to transport anisotropy and geometrical factors. For the nanoribbon structures universal conductance fluctuations were observed. By performing a Fourier transform of the fluctuation pattern a series of distinct phase-coherent closed-loop trajectories are identified. The corresponding enclosed areas can be explained in terms of nanoribbon dimensions and phase-coherence length. In addition, from measurements at different magnetic field tilt angles we can deduce that the area enclosed by the loops are predominately oriented parallel to the quintuple layers.

Supplementary material for this article is available [online](#)

Keywords: topological insulators, phase-coherent transport, selective-area growth, weak antilocalization, nanoribbons

(Some figures may appear in colour only in the online journal)

1. Introduction

Nanoribbons of topological insulators (TI) have attracted considerable interest recently, in particular, since in combination with superconducting contacts spatially separated Majorana

excitations are expected to be realized for the purpose of preparing robust topological quantum bits [1–3]. In this context the understanding of coherent quantum transport in such TI nanoribbons is of paramount importance, particularly in connection with the topologically protected surface states [4–6]. So far most studies in this direction have been performed on ribbons which have been grown epitaxially in a bottom-up approach from the gaseous phase [7–13]. In such ribbons well-developed Aharonov–Bohm (AB) oscillations due to magneto-transport within the topologically protected surface states occurred [7, 9–17]. The two-dimensional nature of the surface states in nanoribbons was confirmed

⁴ These authors contributed equally to this work.



Original Content from this work may be used under the terms of the [Creative Commons Attribution 4.0 licence](#). Any further distribution of this work must maintain attribution to the author(s) and the title of the work, journal citation and DOI.

by observing Shubnikov–de Haas oscillations [14, 18, 19], while phase-coherent transport was revealed by the presence of conductance fluctuations and weak antilocalization [12, 13, 20, 21].

With respect to more circuit flexibility in networks of nanoribbons for topological quantum computation a planar arrangement of these structures prepared by lithography in a top-down process would be advantageous, as compared to the standard bottom-up approach of preparing single free standing nanoribbons. In order to achieve this goal, we fabricated planar $(\text{Bi}_{0.57}\text{Sb}_{0.43})_2\text{Te}_3$ nanoribbons which are grown selectively by molecular beam epitaxy (MBE) within lithographically patterned nano-grooves. This particular stoichiometry was chosen in order to minimize the bulk conductivity contribution [22]. In the selectively grown nanoribbons the van der Waals bonded quintuple layers are oriented parallel to the nanoribbon axis. Thus, current transport between contacts at both ends of the ribbon occurs parallel to the quintuple layers.

For designing circuits for topological quantum computation it is important to know on which length scale phase coherence is maintained, i.e. particularly if interference effects in loop structures are involved [23]. Information on phase-coherence can be obtained by analyzing transport phenomena such as weak (anti)localization and universal conductance fluctuations in structures of the according length scale [24]. The results are immediately applicable to the requirements that have to be matched when moving towards topological insulator based quantum computing architectures.

The coherent quantum magnetotransport is governed by self-interference of electron partial waves in an ensemble of closed-loop trajectories of different size. The loops are formed by elastic scattering at randomly distributed impurities. In the case of weak localization, the constructive interference of time-reversed paths results in an enhanced resistance at zero magnetic field, whereas in the presence of spin–orbit coupling weak antilocalization with an according resistance dip is found [25, 26]. For nano-scaled disordered samples with just a finite number of scattering centers only a few closed-loops Λ are present. Since all of these loops have a different cross section \vec{S}_Λ with respect to the magnetic field \vec{B} , each particular loop Λ acquires a different phase shift due to the different encircled flux Φ_Λ . According to the Aharonov–Bohm effect the conductance contribution of each closed loop will be periodic with the magnetic flux quantum $\Phi_0 = h/e$: $G(\Phi_\Lambda) = G(\Phi_\Lambda + \Phi_0)$. Since each loop has a different cross-section \vec{S}_Λ and thus encircles a different flux the corresponding magnetic field period ΔB_Λ is also different for each loop. As a result, the superposition of oscillations with different periods leads to a fluctuating magneto-conductance pattern [27, 28]. The fluctuation pattern is individual but reproducible for each sample. Vice versa, distinct features observed in the frequency spectrum of the magnetoconductance can be directly assigned to closed loops with a well-determined cross section \vec{S}_Λ with respect to a given magnetic field orientation [29].

Following the conceptual framework of phase-coherent transport, as outlined above, we performed transport measurements on selectively-grown $(\text{Bi}_{0.57}\text{Sb}_{0.43})_2\text{Te}_3$ Hall

bar structures as well as on nanoribbons. The phase-coherence length l_ϕ as a figure-of-merit for phase-coherent transport was extracted by analyzing the weak antilocalization effect. By varying the tilt angle of the magnetic field with respect to the layer surface information on the anisotropy of l_ϕ is gained. In nanoribbons we were able to systematically trace single phase-coherent loops by analyzing universal conductance fluctuations at different tilt angle of the magnetic field [30]. By means of the corresponding Fourier spectra detailed information on size and orientation of these loops is gained.

2. Experimental

Hall bars and nanostructures have been fabricated by MBE using selective-area growth [31, 32]. In figure 1(a) a schematic of the sample layout is shown. For substrate preparation, first, a silicon wafer with a (111) surface orientation is covered with a 5.8 nm thick thermally-grown SiO_2 layer. Subsequently, a 25 nm thick amorphous Si_3N_4 layer is deposited on top using low pressure chemical vapour deposition. A lithographic mask allows to etch the desired structures by reactive ion etching (CHF_3/O_2) and a hydrofluoric acid wet etching step. This etching procedure allows for smooth and crystalline silicon surface areas in the etched regions of the growth mask. The 29 nm thick topological insulator film was grown selectively by means of MBE on the $\text{Si}(111)$ surface at a temperature of 370°C . The temperature window for selective area growth within the mask opening, where no deposition on the mask surface takes place is remarkably small, i.e. of $365^\circ\text{C} < T < 375^\circ\text{C}$. The growth parameters were adjusted such that the stoichiometric composition of the material $(\text{Bi}_{0.57}\text{Sb}_{0.43})_2\text{Te}_3$ is grown [22]. An in-situ capping was achieved by depositing 2 nm of Al that oxidized once exposed to air [33]. A scanning electron micrograph of the cross section of a 50 nm wide nanoribbon prepared by focused ion beam is shown in figure 1(b).

The Ohmic contacts composed of a 5 nm thick Nb layer and a 100 nm thick Au layer were sputtered on top of the TI after removing the AlO_x capping in the contact areas by wet chemical etching and argon sputtering. The Nb is used as a sticking layer. It should be mentioned that neither in previous experiments nor in our experiments any evidence for superconductivity effects caused by this sticking layer were observed. We therefore assume that the contacts carry pure normal conductivity. Hall bars were prepared for characterization of the $(\text{Bi}_{0.57}\text{Sb}_{0.43})_2\text{Te}_3$ film, while the phase-coherent transport was investigated in nanoribbons. Scanning electron micrographs of a contacted nanoribbon and of a Hall bar structure fabricated by selective area growth are shown in figures 1(c) and S1 (supplementary information (stacks.iop.org/Nano/31/325001/mmedia)), respectively.

For magnetotransport measurements a variable temperature insert equipped with a 14 T magnet was employed. The samples were measured at temperatures between 1.4 and 35 K. In order to vary the magnetic field angle a rotating sample holder was employed. The electrical measurements

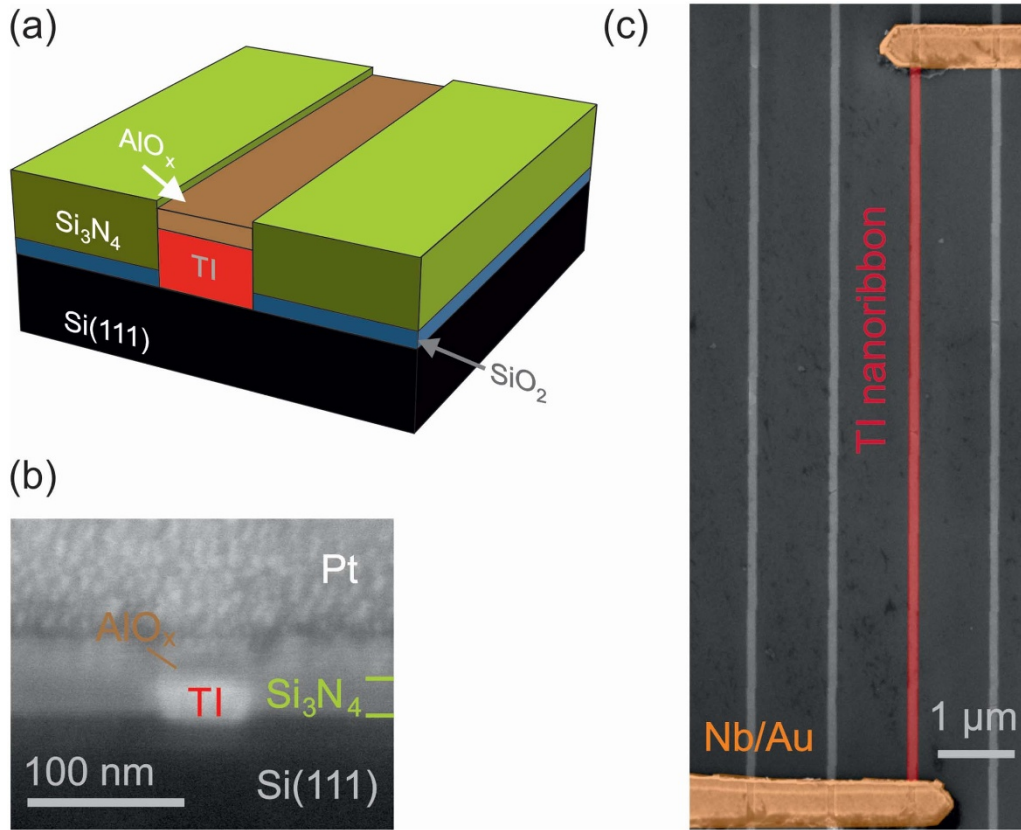


Figure 1. (a) Schematic illustration of a selectively-grown topological insulator (TI) nanoribbon. The nanoribbon is capped by a thin aluminum oxide layer. (b) Scanning electron micrograph of a focused ion beam cut cross section of a 50 nm wide nanoribbon. The silicon oxide layer is not resolved due to its low thickness and the elementary similarity to the substrate. By comparing the lower edge of the TI and the nitride its location can be assumed. On top of the structure platinum layers were deposited by two different techniques in order to stabilize the structure during the cutting procedure. The lower layer of platinum blends into the oxide capping and the nitride layers visually. (c) Scanning electron beam micrograph of a contacted 100 nm wide nanoribbon (indicated in red). The neighboring nanoribbons do not contribute to the transport.

were performed by using lock-in technique and injecting an AC current of 10 nA into the nanoribbon.

3. Results and discussion

3.1. Hall bar structures

In order to characterize the transport properties of the $(\text{Bi}_{0.57}\text{Sb}_{0.43})_2\text{Te}_3$ film, first, magnetoresistance and Hall effect measurements were performed on a Hall bar structure with a length of 100 μm and a width of 10 μm. In figure 2(a) the magnetoresistance at temperatures ranging from 4 to 35 K is shown.

The magnetic field is oriented perpendicular to the TI layer. The magnetoconductance curves reveal a positive magnetoresistance with a distinct dip at zero magnetic field, which can be attributed to weak antilocalization [25, 26, 34], as it was reported for Bi_2Se_3 [35–37], Bi_2Te_3 [22, 38, 39], Sb_2Te_3 [40, 41], as well as for $(\text{Bi}_x\text{Sb}_{1-x})_2\text{Te}_3$ layers [22]. As can be seen in figure 2(a), inset, the Hall voltage has a linear negative slope, which indicates that the transport is *n*-type [22]. From magnetoresistance and Hall measurements a resistivity

of $\rho = 2.5 \times 10^{-3} \Omega \text{ cm}$, a projected 2D carrier concentration of $1.02 \times 10^{14} \text{ cm}^{-2}$, and a mobility of $139 \text{ cm}^2/\text{Vs}$ at a temperature $T = 4 \text{ K}$ were extracted. The relatively large charge carrier concentration indicates a considerable contribution of bulk charge carriers participating in the transport [22]. From the above values an elastic mean free path of $l_e = 6 \text{ nm}$ was derived. By increasing the temperature from 4 to 35 K, the electron concentration only increases slightly, by less than 3%, showing that the transport is in the metallic regime. In order to gain information on phase-coherent transport from the weak antilocalization feature a fit to the Hikami–Larkin–Nagaoka (HLN) model was performed (see figure S2) [25]. From the fit a phase-coherence length l_ϕ of about 150 nm was extracted at 4 K. The temperature dependent decay was found to be proportional to $T^{-0.5}$ which is in agreement with the Nyquist electron-electron interaction for disordered systems [42]. Furthermore, we find that the transport takes place in a single channel, since the fitted pre-factor α of the HLN formula of about -0.4 is close to the predicted value of -0.5 for a single channel. This suggests an interpretation of two topological two-dimensional transport channels that are coupled via bulk scattering, or alternatively that device fabrication causes the two channels to have substantially different phase-coherence lengths [22, 43]. In addition,

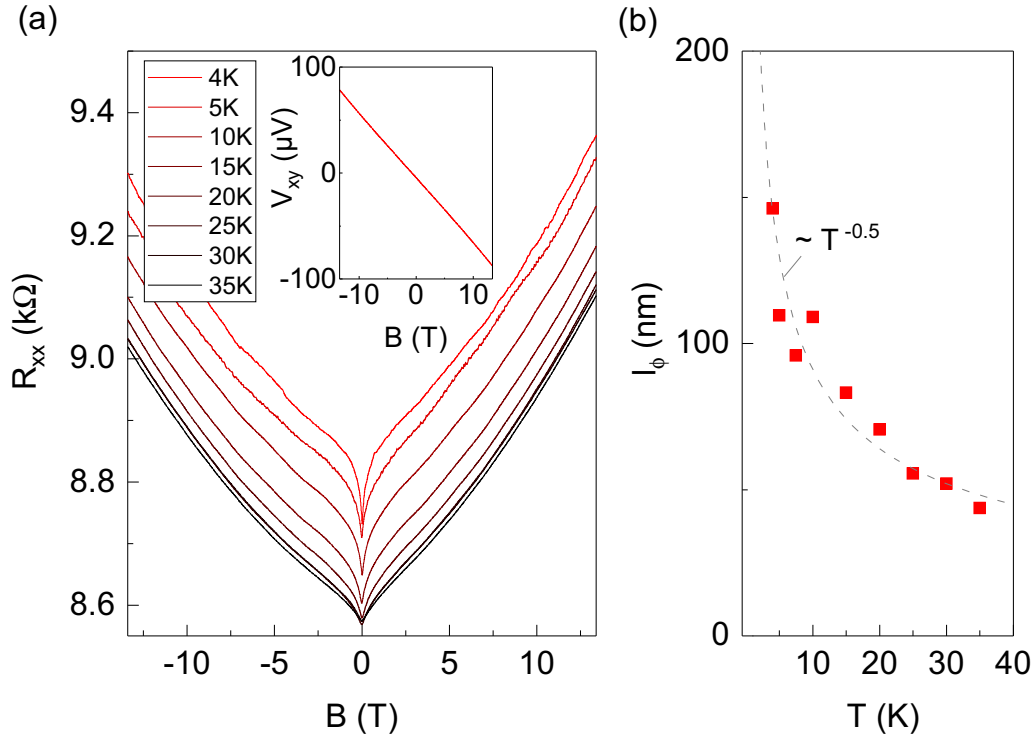


Figure 2. (a) Magnetoconductance of a Hall bar structure measured at temperatures ranging from 4 to 35 K. The inset shows the corresponding Hall voltage V_{xy} at 4 K. (b) Phase-coherence length l_ϕ as a function of temperature extracted from the weak antilocalization measurements. The gray line corresponds to the fit with a temperature dependence according to $l_\phi \propto T^{-0.5}$. l_ϕ was obtained by performing a Hikami–Larkin–Nagaoka fit to the data.

the presence of a two-dimensional electron gas containing massive electrons (parabolic dispersion) due to charge accumulation at the surfaces could lead to another two-dimensional transport channel [44–46].

3.2. Nanoribbons

We now turn to the transport experiments on a selectively-grown nanoribbon with a length of $10\ \mu\text{m}$, a width of $50\ \text{nm}$, and a thickness of $29\ \text{nm}$. The measurements were performed in a two-terminal configuration at a temperature of $1.4\ \text{K}$. In figure 3 the magnetoresistance is shown as a function of tilt angle θ of the magnetic field. The sample shows a resistance of about $440\ \text{k}\Omega$ at $0\ \text{T}$, corresponding to a resistivity of $\rho = 6.4 \times 10^{-3}\ \Omega\text{cm}$. We attribute the higher resistivity compared to values obtained from the Hall bar measurements to the additional boundary scattering contribution.

As found in the measurements on Hall bar structures, the curves possess a dip feature at zero magnetic field due to the weak antilocalization effect. In addition to what has been observed in the Hall measurements, one finds reproducible resistance modulations, which will be addressed in detail below. This feature was observed in all nanoribbons under investigation, i.e. a set of measurements on a nanoribbon with a width of $100\ \text{nm}$ is shown in figure S3. The resistance modulations only occur in nanostructures and get lost in the transition to microstructures. Since the phase-coherence length l_ϕ extracted from the Hall bar measurements exceeds the ribbon width

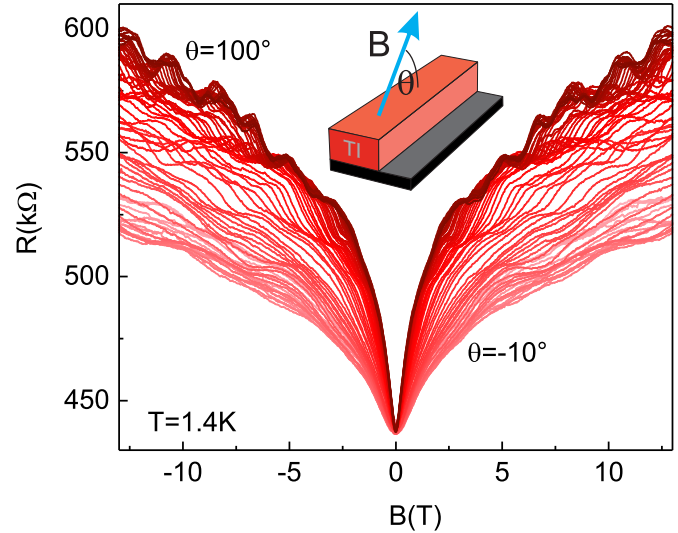


Figure 3. Magnetoresistance of a $10\ \mu\text{m}$ long and $50\ \text{nm}$ wide nanoribbon at different tilt angles of the magnetic field. The measurements were performed at $1.4\ \text{K}$. The measurements from $\theta = -10^\circ$ to 10° were done at a stepping of 1° , from $\theta = 10^\circ$ to $\theta = 100^\circ$ a stepping of 2° was chosen. The inset shows the orientation of the magnetic field B with respect to the upper surface of the ribbon.

we applied a model for quasi 1-dimensional structures to fit the experimental data and to extract l_ϕ [42, 47, 48]. For dirty metals in the strong spin-orbit scattering limit the correction of

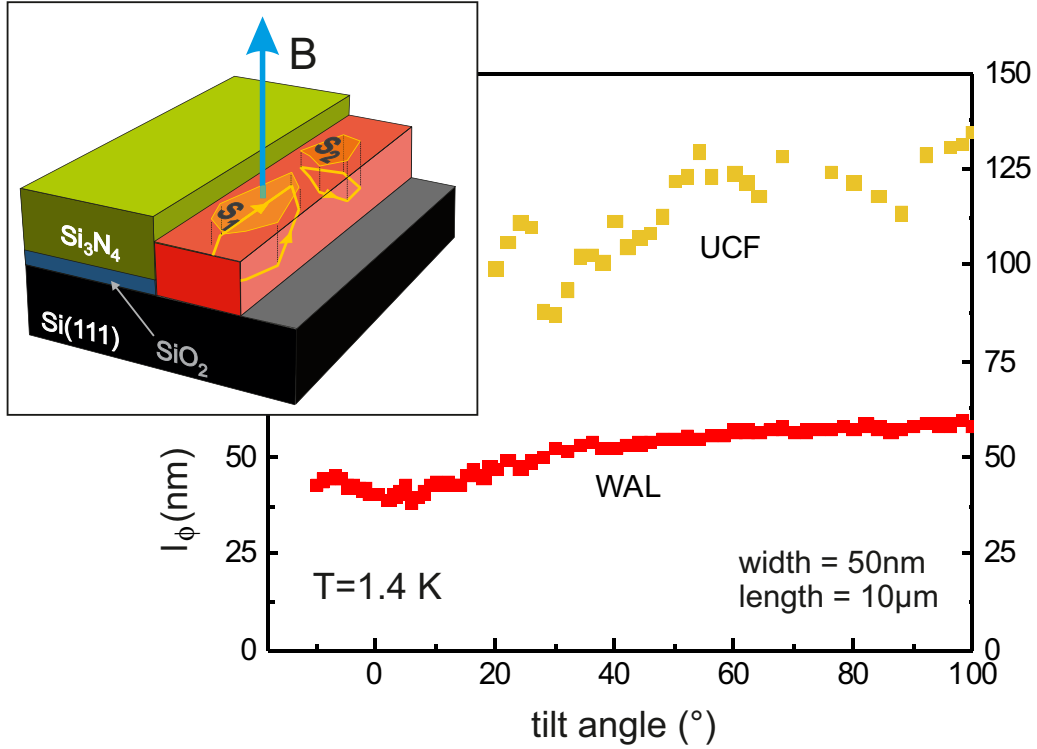


Figure 4. Phase-coherence length in the nanoribbon as a function of tilt angle of the magnetic field for WAL by fitting the experimental data shown in figure 3 according to equation (1) (red symbols) and from UCF theory (yellow symbols) applied to the same data. Inset: Schematic arrangement of the nanoribbon with two exemplary closed loops and their projected enclosed areas S_1 and S_2 with respect to a perpendicular magnetic field B .

the resistance due to weak antilocalization can be expressed by a quasiclassical approach [49]

$$\Delta R = -\frac{1}{2} \frac{R^2}{L} \frac{e^2}{\pi \hbar} \left(\frac{1}{l_\phi(\theta)^2} + \frac{1}{l_{B,\perp}(\theta)^2} + \frac{1}{l_{B,\parallel}(\theta)^2} \right)^{-1/2}. \quad (1)$$

Here, l_ϕ is the phase-coherence length at a tilt angle θ ; w and d are the width and thickness of the ribbon, respectively, and L is the contact separation. Furthermore, the magnetic dephasing lengths for the perpendicular and parallel components of the magnetic field are defined as $l_{B,\perp} = \sqrt{3\hbar}/eB \sin(\theta)w$ and $l_{B,\parallel} = \sqrt{2\pi\hbar}/eB \cos(\theta)\sqrt{wd}$, respectively [42, 47, 49]. These parameters take care of the geometrical limitations in different orientations. A possible contribution of the Zeeman effect was neglected, since it could be shown by weak localization measurements on topological insulator layers that this contribution is not relevant in the low field range [36, 50]. The model was fitted to the data for the different sample orientations. A typical fit is shown in figure S4. Figure 4 shows the results of the fit (red symbols). For a magnetic field aligned perpendicularly to the substrate plane ($\theta = 90^\circ$) we find a phase-coherence length of around 60 nm, which is reduced by 30% to about 40 nm for an in-plane magnetic field. Thus, an angular dependence of l_ϕ is extracted from the WAL. This indicates an anisotropy of the material favouring coherent transport parallel to the substrate surface [32, 51]. As a matter of fact for similar measurements on InAs nanowires it was found that l_ϕ is rather constant which shows that here no anisotropy is present [49]. Nevertheless, we

cannot completely rule out that the angular dependence of l_ϕ is also affected by geometrical factors [52]. The phase-coherence length of around 60 nm for a perpendicular field is somewhat smaller than the value gained from the Hall bar structure. A possible reason might be the effect of boundary scattering on the phase-coherence length in case of the nanoribbon.

The modulations of the magnetoresistance $R(B)$ found in figure 3 can be attributed to universal conductance fluctuations [27, 28]. As mentioned above, these fluctuations originate from the Aharonov–Bohm type interference of closed-loop electron trajectories of different size and orientation (see schematic illustration in figure 4) [29]. By analyzing the correlation field B_C of the conductance fluctuations the characteristic phase-coherence length for the interference in the loops can be estimated [27, 53]. The correlation field is determined via the autocorrelation function $F(\Delta B) = \langle \delta G(B + \Delta B) \delta G(B) \rangle$ by $F(B_C) = \frac{1}{2} F(0)$. Here, $\delta G(B)$ are the conductance fluctuations after subtracting the slowly varying background and $\langle \dots \rangle$ denotes the average over the magnetic field. For a quasi-one-dimensional transport channel in the dirty limit $l_e \ll w$ the relation between B_C and l_ϕ is expressed by $B_C = \gamma \Phi_0 / (l_\phi w)$ [53, 54]. For the prefactor γ we choose 0.42 [54] for l_ϕ larger than the thermal length $l_T = \sqrt{\hbar \mathcal{D} / k_B T} \approx 7$ nm, with \mathcal{D} the diffusion constant calculated from the mobility and the charge carrier concentration. In figure 4 the phase-coherence length l_ϕ extracted from B_C is plotted for different tilt angles θ . We restricted the analysis to tilt angles $\theta \geq 20^\circ$ since for smaller values of θ too few

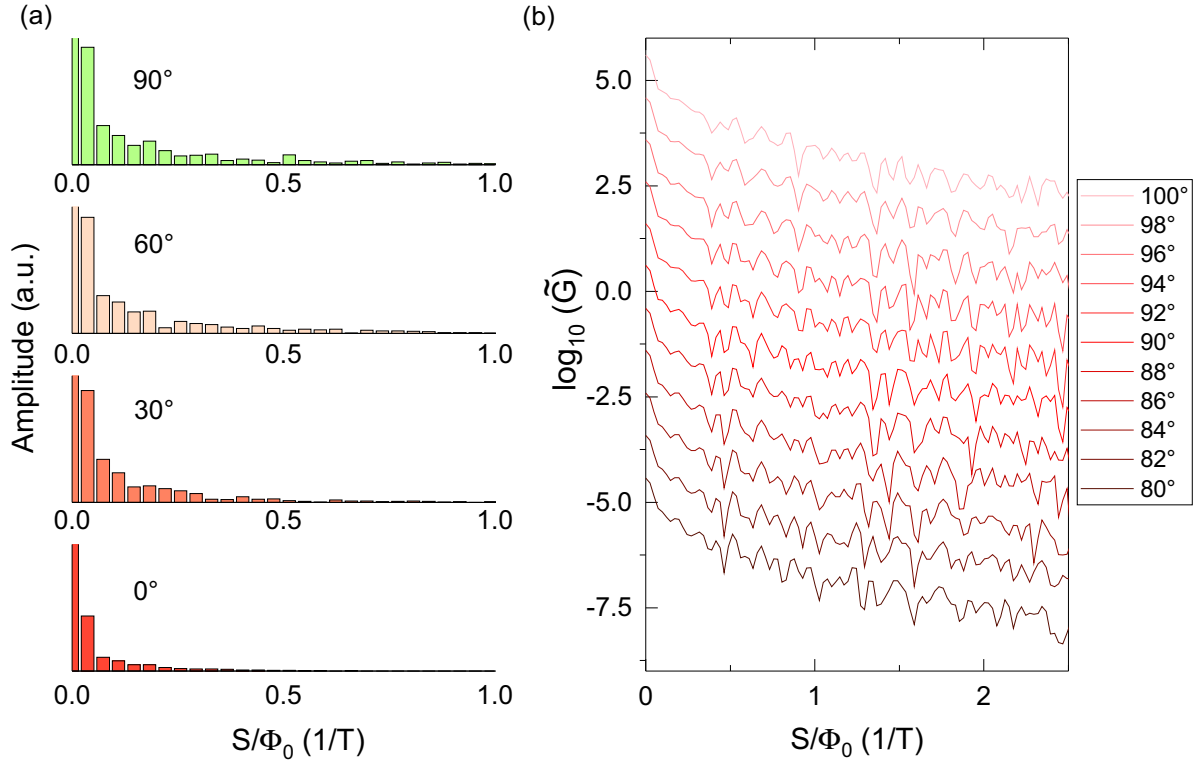


Figure 5. (a) Fourier amplitude vs. loop cross sectional area per magnetic flux quantum S/Φ_0 for magnetic field tilt angles of 0° , 30° , 60° , and 90° . (b) Logarithm of the Fourier amplitude $\log_{10}(\tilde{G})$ vs. S/Φ_0 taken from the magnetoconductance at magnetic field tilt angles between 80° and 100° . The data is plotted with an offset for better visibility. The bottom curve is without offset.

fluctuations occurred in the measured magnetic field range. Once again we find a tendency that l_ϕ is anisotropic, i.e. l_ϕ is smaller for small tilt angles, similar to our analysis of the WAL measurements. However, the values of l_ϕ obtained from the UCF measurements are larger by a factor of about two compared to the values gained from the WAL measurements. The significant difference between the two l_ϕ values might have several reasons. First, the l_ϕ values evaluated from UCFs originate from measurements in large magnetic fields, in contrast to WAL where l_ϕ is determined close to zero magnetic field. Consequently, spin-related scattering mechanisms might yield differently strong contributions in both phenomena. Second, there might be uncertainties in the theoretical analysis of both interference phenomena, e.g. the characteristic γ factor in the UCF analysis might deviate from the theoretically predicted value [52]. Third, the phase-coherence length l_ϕ is in the order of the circumference of the nanoribbon. In that case the interference effects in the magnetoconductance are also limited by the circumference in addition to l_ϕ [55].

For the universal conduction fluctuations each individual loop contributes to the magnetoconductance with a characteristic period and thus with a particular frequency. Therefore, by analyzing the frequency spectrum of the magnetoconductance detailed information on the loop sizes, i.e. cross sections \tilde{S}_Λ with respect to an applied magnetic field \vec{B} , can be obtained. In order to do so, we calculated the Fourier transform of the magnetoconductance $G(B) = 1/R(B)$:

$$\tilde{G}(S/\Phi_0) = \int dB G(B) \exp(-2\pi i B S/\Phi_0), \quad (2)$$

with S the loop cross sectional area perpendicular to a given orientation of an applied magnetic field. Figure 5(a) gives an overview of the Fourier amplitude vs. S/Φ_0 ('frequency') in units of $1/T$ at a magnetic field tilt of 0° , 30° , 60° , and 90° , respectively. The Fourier amplitude generally decreases with increasing S/Φ_0 , which reflects the fact that the loop return probability decreases with increasing loop size. Furthermore, towards larger tilt angles the frequency range is extended. This can be explained by the larger allowed projection areas provided for loops at larger tilt angles.

In order to resolve more details in the Fourier spectrum, the logarithm of the Fourier amplitude $\log_{10}(\tilde{G})$ as a function of S/Φ_0 is plotted in figure 5(b) for tilt angles between 80° and 100° . No background was subtracted from the original signal. It is clear that the Fourier spectrum fluctuates indicating that it contains a large number of different frequencies. The spectrum reflects the contribution of different loops with specific cross sectional areas S to the magnetoconductance. The spectrum is reproducible, and changes gradually when the magnetic field orientation is varied. These changes occur because as the tilt angle changes, each loop's cross-sectional area perpendicular to the magnetic field vector also changes.

Collecting the traces corresponding to different magnetic field orientations in a color plot confirms that there are systematic patterns in the fluctuations of the Fourier spectrum, as shown in figure 6(a).

One can clearly see that for a perpendicular magnetic field the oscillation frequency range is large whereas for a parallel

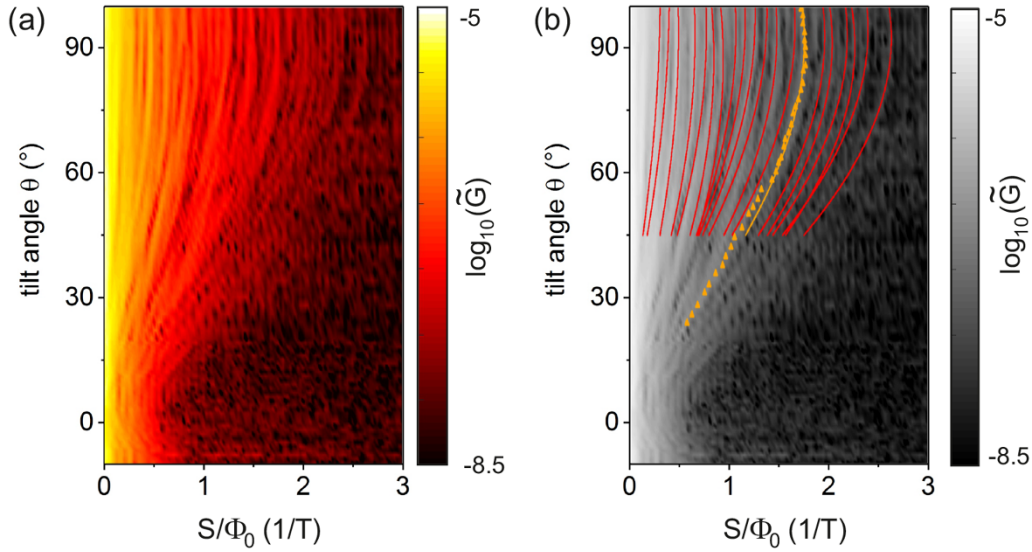


Figure 6. (a) Color plot of the logarithm of the Fourier amplitude $\log(\tilde{G})$ of the magnetoconductance of the nanoribbon as a function of loop cross sectional area per flux S/Φ_0 and the magnetic field tilt angle. (b) Corresponding gray-scale plot with an exemplary sequence of dots tracing peaks in the spectrum while the tilt angle changes. The red lines are fits to different dot sequences according to equation (3).

magnetic field the range is considerably smaller, i.e. the characteristic brighter stripes are getting closer towards smaller magnetic field tilt angles θ . Since the frequency is directly proportional to the loop cross sectional area S with respect to the magnetic field orientation, one can directly deduce that for the perpendicular case larger-area loops contribute. This is indeed plausible, since for that orientation, the maximum phase-coherent loop area is approximately given by $S = l_\phi w$, with l_ϕ the phase-coherence length and w the nanoribbon width, assuming $w < l_\phi$. One finds that at $\theta = 90^\circ$ the frequency contributions diminish at about 2.5 T^{-1} corresponding to an area of approximately 10^4 nm^2 resulting in a lower estimate for the phase-coherence length l_ϕ of 200 nm. This value is close but somewhat larger than the corresponding value determined from the correlation field. For the parallel magnetic field orientation the maximum loop area is given by the cross section $S = wd = 1450 \text{ nm}^2$ of the ribbon, providing that the thickness d of the $(\text{Bi}_{0.57}\text{Sb}_{0.43})_2\text{Te}_3$ layer is smaller than l_ϕ . The corresponding value of $S/\Phi_0 = 0.35 \text{ T}^{-1}$ fits very well to the range found in figure 6(a) at $\theta = 0$. However, we do not find a distinct single Aharonov–Bohm peak in the spectrum at 0.35 T^{-1} , as it would be expected if the transport solely takes place in the topologically protected surface states or in the accumulation layer of massive electrons at the interface. One reason might be that the thickness of the nanoribbons varies by one or two quintuple layers, resulting in a variation of the cross-section along the ribbon. We furthermore observe some frequency contributions below 0.35 T^{-1} indicating that smaller size loops in the bulk contribute as well.

As mentioned above, in figure 6(a) we find a stripe-like pattern of peaks in the Fourier spectrum which is getting closer towards smaller tilt angles. Each stripe can be assigned to a distinct phase-coherent loop [29]. In order to gain more precise information on the loop orientation with respect to the magnetic field we followed each trace and determined a

set of corresponding discrete points in the $S/\Phi_0 - \theta$ plane, as indicated exemplarily by the orange dots in figure 6(b). To each sequence of data points we performed a fit according to

$$\frac{S_\Lambda(\theta)}{\Phi_0} = \frac{S_{\Lambda,\max}}{\Phi_0} \sin(\theta + \gamma_\Lambda), \quad (3)$$

with $S_\Lambda(\theta)$ and $S_{\Lambda,\max}$ the projected and maximum loop area, respectively, while γ_Λ is the tilt angle of the maximum loop area with respect to the substrate plane. Some exemplary fits are shown in figure 6(b) (red lines).

We find that most of the lines correspond to loops with small tilt angles γ_Λ in the range of $\pm 7^\circ$. In fact, we could not identify any sine-like lines with larger offset angles γ_Λ , corresponding to loops with a larger tilt angle. This is indeed remarkable, since if we would assume bulk conductance, phase-coherent loops with orientations in a much broader range of tilt angles are expected. This is particularly true for loops enclosing a smaller area, since here the tilt angle should not be limited by geometrical constraints, i.e. the elongated shape of the ribbon. Thus, we can state that the peaks found in the Fourier spectrum correspond to interference loops that are mainly oriented within the plane parallel to the substrate. Most likely, these loops are located within the topologically protected surface states. However, from the fact that we find loops with finite tilt angles, we can also infer that the phase-coherent loops extend over different quintuple layers to a certain extent, i.e. the weak van der Waals bonding does not prevent an extension of the electron waves across the quintuple layers, completely [32]. In the supplementary information, we support our conclusions drawn here, by modelling the Fourier spectrum for a typical set of loops and deducing from that the magnetoconductance fluctuations.

Finally, let us briefly come back to the general properties of the Fourier spectrum. As shown in figure 5(a), the amplitude in the Fourier spectrum is generally decreasing with increasing

projected loop area S/Φ_0 . Thus, the number of coherent loops with a certain projection area is decreasing for increasing loop sizes. This general trend reflects the fact that the return probability decreases the more the electron trajectories move away from their origin. Including all contributing loops leads to the observed weak antilocalization feature [29]. However, owing to the small dimensions of the nanoribbon and the according finite number of loops there is a randomness in the actual distribution of the loop sizes. This finally results in the superimposed fluctuations in the amplitude of the Fourier spectrum and the stripe pattern when plotted as a function of tilt angle (cf figure 6). The fact, that the stripe pattern systematically shifts with the tilt angle supports our interpretation that the orientation of all loops contributing to a certain Fourier amplitude is basically the same, i.e. parallel to the quintuple layers. If this would not be the case, the fluctuation pattern would not be shifted systematically but rather randomly.

4. Conclusions








In conclusion, by using selective-area molecular beam epitaxy we succeeded to grow $(\text{Bi}_{0.57}\text{Sb}_{0.43})_2\text{Te}_3$ topological insulator Hall bar structures as well as nanoribbons. Low temperature magnetotransport experiments on these structures revealed signatures of weak antilocalization. From these measurements a phase-coherence length in the order of 100 nm was extracted. By performing measurements in a tilted magnetic field we extracted a phase-coherence length which is larger for loops oriented parallel to the quintuple layers. This behaviour is attributed to transport anisotropy and geometrical factors. For the nanoribbons we also observed universal conductance fluctuations. By performing a Fourier transform of the fluctuation pattern we were able to identify a series of distinct phase-coherent closed-loop trajectories with areas which can be explained in terms of nanoribbon dimensions and phase-coherence length. From measurements at different magnetic field tilt angles we conclude that these loops are predominately located parallel to the quintuple layers i.e. within the topologically protected surface states.

We expect that the present approach towards analyzing universal conductance fluctuations at different magnetic field orientations by Fourier transforms turns out to be a powerful tool for better understanding conducting pathways in disordered topological materials and nanostructures thereof. In the present samples, we could not avoid a significant bulk conductance contribution due to background doping. In future structures, one should try to minimize the impact of background doping either by using optimized ternary or quaternary topological insulators and by means of heterostructures or by gate control. Latter could also help to avoid a possible two-dimensional contribution of massive electrons from the conduction band in the surface accumulation layer. If that is once achieved it should be possible to observe a single peak in the Fourier spectrum for an in-plane magnetic field resulting from Aharonov–Bohm type oscillations due to phase-coherent transport in the topologically protected surface states.

Acknowledgments

We thank Herbert Kertz for technical assistance. This work was supported by the Virtual Institute for Topological Insulators (VITI), which is funded by the Helmholtz Association. This work was partly funded by the Deutsche Forschungsgemeinschaft (DFG, German Research Foundation) under Germany's Excellence Strategy - Cluster of Excellence Matter and Light for Quantum Computing (ML4Q) EXC 2004/1 - 390 534 769. VES thanks S. Blügel, the Peter Grünberg Institute, and S. Kettemann for hospitality.

ORCID iDs

Jonas Kölzer  <https://orcid.org/0000-0003-3312-9671>
 Daniel Rosenbach  <https://orcid.org/0000-0002-1824-7293>
 Peter Schüffelgen  <https://orcid.org/0000-0001-7977-7848>
 Gregor Mussler  <https://orcid.org/0000-0001-7230-0756>
 Detlev Grützmacher  <https://orcid.org/0000-0001-6290-9672>
 Hans Lüth  <https://orcid.org/0000-0003-1617-3355>
 Thomas Schäpers  <https://orcid.org/0000-0001-7861-5003>

References

- [1] Cook A and Franz M 2011 Majorana fermions in a topological-insulator nanowire proximity-coupled to an *s*-wave superconductor *Phys. Rev. B* **84** 201105
- [2] Manousakis J, Altland A, Bagrets D, Egger R and Ando Y 2017 Majorana qubits in a topological insulator nanoribbon architecture *Phys. Rev. B* **95** 165424
- [3] Schüffelgen P *et al* 2019 Selective area growth and stencil lithography for in situ fabricated quantum devices *Nat. Nanotechnol.* **14** 825–31
- [4] Bardarson J H, Brouwer P W and Moore J E 2010 Aharonov-Bohm oscillations in disordered topological insulator nanowires *Phys. Rev. Lett.* **105** 156803
- [5] Zhang Y and Vishwanath A 2010 Anomalous Aharonov-Bohm conductance oscillations from topological insulator surface states *Phys. Rev. Lett.* **105** 206601
- [6] Sacksteder V E and Quansheng W 2016 Quantum interference effects in topological nanowires in a longitudinal magnetic field *Phys. Rev. B* **94** 205424
- [7] Peng H, Lai K, Kong D, Meister S, Chen Y, Xiao-Liang Q, Zhang S-C, Shen Z-X and Cui Y 2010 Aharonov-Bohm interference in topological insulator nanoribbons *Nat. Mater.* **9** 225–9
- [8] Yan Y, Liao Z-M, Zhou Y-B, Han-Chun W, Bie Y-Q, Chen J-J, Meng J, Xiao-Song W and Da-Peng Y 2013 Synthesis and quantum transport properties of Bi_2Se_3 topological insulator nanostructures *Sci. Rep.* **3** 1264
- [9] Hamdou B, Gooth J, Dorn A, Pippel E, and Nielsch K 2013 Aharonov-Bohm oscillations and weak antilocalization in topological insulator Sb_2Te_3 nanowires *App. Phys. Lett.* **102** 22
- [10] Hong S S, Zhang Y, Cha J J, Xiao-Liang Q and Cui Y 2014 One-dimensional helical transport in topological insulator nanowire interferometers *Nano Lett.* **14** 2815–21
- [11] Jauregui L A, Pettes M T, Rokhinson L P, Shi Li and Chen Y P 2016 Magnetic field-induced helical mode and topological transitions in a topological insulator nanoribbon *Nat. Nanotechnol.* **11** 345
- [12] Arango Y C, Huang L, Chen C, Jose Avila M C Asensio D G, Lüth H, Lu J G and Thomas S 2016 Quantum transport and

- nano angle-resolved photoemission spectroscopy on the topological surface states of single Sb_2Te_3 nanowires *Sci. Rep.* **6** 29493
- [13] Dufouleur J *et al* 2017 Weakly-coupled quasi-1d helical modes in disordered 3d topological insulator quantum wires *Sci. Rep.* **7** 45276
- [14] Xiu F *et al* 2011 Manipulating surface states in topological insulator nanoribbons *Nat. Nanotechnol.* **6** 216–21
- [15] Tian M, Ning W, Zhe Q, Haifeng D, Wang J and Zhang Y 2013 Dual evidence of surface dirac states in thin cylindrical topological insulator Bi_2Te_3 nanowires *Sci. Rep.* **3** 1212
- [16] Cho S, Dellabetta B, Zhong R, Schneeloch J, Liu T, Genda G, Gilbert M J and Mason N 2015 Aharonov-Bohm oscillations in a quasi-ballistic three-dimensional topological insulator nanowire *Nat. Commun.* **6**
- [17] Ziegler J *et al* 2018 Probing spin helical surface states in topological HgTe nanowires *Phys. Rev. B* **97** 035157
- [18] Fang L, Jia Y, Miller D J, Latimer M L, Xiao Z L, Welp U, Crabtree G W and Kwok W-K 2012 Catalyst-free growth of millimeter-long topological insulator Bi_2Se_3 nanoribbons and the observation of the π -berry phase *Nano Lett.* **12** 6164–9
- [19] Gooth J, Hamdoun B, Dorn A, Zierold R and Nielsch K 2014 Resolving the dirac cone on the surface of Bi_2Te_3 topological insulator nanowires by field-effect measurements *Appl. Phys. Lett.* **104** 243115
- [20] Matsuo S *et al* 2012 Weak antilocalization and conductance fluctuation in a submicrometer-sized wire of epitaxial Bi_2Se_3 *Phys. Rev. B* **85** 075440
- [21] Matsuo S *et al* 2013 Experimental proof of universal conductance fluctuation in quasi-one-dimensional epitaxial Bi_2Se_3 wires *Phys. Rev. B* **88** 155438
- [22] Weyrich C *et al* 2016 Growth, characterization and transport properties of ternary $(\text{Bi}_{1-x}\text{Sb}_x)_2\text{Te}_3$ topological insulator layers *J. Phys.: Condens. Matter.* **28** 495501
- [23] Akhmerov A R, Dahlhaus J P, Hassler F, Wimmer M and Beenakker C W J 2011 Quantized conductance at the majorana phase transition in a disordered superconducting wire *Phys. Rev. Lett.* **106** 057001
- [24] Beenakker C W J and van Houten H 1991 Quantum transport in semiconductor nanostructures *Solid State Phys.* **44** 1–228
- [25] Hikami S, Larkin A I and Nagaoka Y 1980 Spin-orbit interaction and magnetoresistance in the two dimensional random system *Prog. Theor. Phys.* **63** 707–10
- [26] Bergmann G 1984 Weak localization in thin films, a time-of-flight experiment with conduction electrons *Phys. Rep.* **107** 1–58
- [27] Lee P A and Stone A D 1985 Universal conductance fluctuations in metals *Phys. Rev. Lett.* **55** 1622–5
- [28] Al'tshuler B L 1985 Fluctuations in the extrinsic conductivity of disordered conductors *Pis'ma Zh. Eksp. Teo. Fiz.* **41** 530–3
- [29] Sacksteder V 2018 Fermion loops, linear magnetoresistance, linear in temperature resistance, and bad metals arXiv 1801.02663
- [30] Jespersen T S, Hauptmann J R, Sørensen C B and Nygård J 2015 Probing the spatial electron distribution in InAs nanowires by anisotropic magnetoconductance fluctuations *Phys. Rev. B* **91** 041302
- [31] Kampmeier J, Weyrich C, Lanius M, Schall M, Neumann E, Mussler G, Schäpers T and Detlev G 2016 Selective area growth of Bi_2Te_3 and Sb_2Te_3 topological insulator thin films *J. Cryst. Growth* **443** 38–42
- [32] Weyrich C, Lanius M, Schüffelgen P, Rosenbach D, Mussler G, Bunte S, Trelenkamp S, Grützmacher D and Thomas S 2019 Phase-coherent transport in selectively grown topological insulator nanodots *Nanotechnology* **30** 055201
- [33] Lang M *et al* 2011 Revelation of topological surface states in Bi_2Se_3 thin films by in situ Al passivation *Acs Nano* **6** 295–302
- [34] Adroguer P, Liu W E, Culcer D and Hankiewicz E M 2015 Conductivity corrections for topological insulators with spin-orbit impurities: Hikami-Larkin-Nagaoka formula revisited *Phys. Rev. B* **92** 241402
- [35] Chen J *et al* 2010 Gate-voltage control of chemical potential and weak antilocalization in Bi_2Se_3 *Phys. Rev. Lett.* **105** 176602
- [36] Chen J, He X Y, Wu K H, Ji Z Q, Lu L, Shi J R, Smet J H and Li Y Q 2011 Tunable surface conductivity in bi_2se_3 revealed in diffusive electron transport *Phys. Rev. B* **83** 241304
- [37] Steinberg H, Laloë J-B, Fatemi V, Moodera J S and Jarillo-Herrero P 2011 Electrically tunable surface-to-bulk coherent coupling in topological insulator thin films *Phys. Rev. B* **84** 233101
- [38] Hong-Tao H, Wang G, Zhang T, Iam-Keong Sou G K, Wong L, Wang J-N, Hai-Zhou L, Shen S-Q and Zhang F-C 2011 Impurity effect on weak antilocalization in the topological insulator Bi_2Te_3 *Phys. Rev. Lett.* **106** 166805
- [39] Chiu S-P and Lin J-J 2013 Weak antilocalization in topological insulator Bi_2Te_3 microflakes *Phys. Rev. B* **87** 035122
- [40] Takagaki Y, Giussani A, Perumal K, Calarco R and Friedland K-J 2012 Robust topological surface states in Sb_2Te_3 layers as seen from the weak antilocalization effect *Phys. Rev. B* **86** 125137
- [41] Taskin A A, Sasaki S, Segawa K and Ando Y 2012 Manifestation of topological protection in transport properties of epitaxial Bi_2Se_3 thin films *Phys. Rev. Lett.* **109** 066803
- [42] Al'tshuler B L and Aronov A G 1981 Magnetoresistance of thin films and of wires in a longitudinal magnetic field *Pis'ma Zh. Eksp. Teor. Fiz.* **33** 515
- [43] Ando Y 2013 Topological insulator materials *J. Phys. Soc. Japan* **82** 102001
- [44] Bianchi M, Guan D, Bao S, Jianli Mi, Iversen B B and Philip D C 2010 King and Philip Hofmann Coexistence of the topological state and a two-dimensional electron gas on the surface of bi_2se_3 *Nat. Commun.* **1** 128
- [45] Brahlek M, Koirala N, Bansal N and Seongshik O 2015 Transport properties of topological insulators: Band bending, bulk metal-to-insulator transition and weak anti-localization *Solid State Commun.* **215216** 54–62
- [46] Mooshammer F *et al* 2018 Nanoscale near-field tomography of surface states on $(\text{Bi}_{0.5}\text{Sb}_{0.5})_2\text{Te}_3$ *Nano Lett.* **18** 7515–23
- [47] Beenakker C W J and van Houten H 1988 Boundary scattering and weak localization of electrons in a magnetic field *Phys. Rev. B* **38** 3232–40
- [48] Kurdak C, Chang A M, Chin A and Chang T Y 1992 Quantum interference effects and spin-orbit interaction in quasi-one-dimensional wires and rings *Phys. Rev. B* **46** 6846–56
- [49] Liang D, Juan D and Gao X P A 2010 Anisotropic magnetoconductance of a InAs nanowire: Angle-dependent suppression of one-dimensional weak localization *Phys. Rev. B* **81** 153304
- [50] Wang X, Xiaoyue H, Guan T, Liao J, Lin C, Kehui W, Yongqing Li and Zeng C 2012 Transport properties of topological insulator Bi_2Se_3 thin films in tilted magnetic fields *Phys. E: Low-Dimen. Sys. Nanostruct.* **46** 236–40
- [51] Yu B, Yavorsky N F, Mertig H, I and Zahn P 2011 Electronic structure and transport anisotropy of Bi_2Te_3 and Sb_2Te_3 *Phys. Rev. B* **84** 165208

- [52] Ch B, M Lepsa I, Luysberg M, Grützmacher D, Lüth H and Th Schäpers 2011 Electronic phase coherence in InAs nanowires *Nano Lett.* **11** 3550–6
- [53] Lee P A, Douglas Stone A and Fukuyama H 1987 Universal conductance fluctuations in metals: Effects of finite temperature, interactions and magnetic field *Phys. Rev. B* **35** 1039–70
- [54] Beenakker C W J and van Houten H 1988 Flux-cancellation effect on narrow-channel magnetoresistance fluctuations *Phys. Rev. B* **37** 6544–6
- [55] Sacksteder V E, Arnardottir K B, Kettemann S and Shelykh I A 2014 Topological effects on the magnetoconductivity in topological insulators *Phys. Rev. B* **90** 235148